Computational study of turbulent natural convection in a side-heated near-cubic enclosure at a high Rayleigh number

H.S. Dol [1], K. Hanjalić *

Applied Physics Department, Delft University of Technology, Lorentzweg 1, 2628 CJ Delft, The Netherlands

Abstract

A computational study of turbulent natural convection in a side-heated near-cubic enclosure at a high Rayleigh number ($Ra = 4.9 \times 10^{10}$) is performed, aimed at gaining a better insight into the flow pattern, particularly in the corner regions. Two types of thermal boundary conditions are applied at the horizontal walls: adiabatic and isothermal. Also, two kinds of lateral vertical walls are studied, corresponding to different experimental approximations of adiabatic conditions: the first by insulation and the second by imposing a stratified wall heating. The latter conditions ensure better flow two-dimensionality, with the temperature stratification on the vertical walls close to that expected in the parallel mid-plane. Computations are performed with both a two-dimensional (2D) and three-dimensional (3D) code using a low-Reynolds-number differential second-moment stress/flux closure and the related k–ε model (KEM) simplification. The numerical computations show that the second-moment closure (SMC) is better in capturing thermal three-dimensionality effects and strong streamline curvature in the corners. The KEM, however, still provides reasonable predictions of the first moments away from the corners. © 2001 Elsevier Science Ltd. All rights reserved.

1. Introduction

The EUROTHERM/ERCOFTAC Workshop "Benchmark Computation and Experiment for Turbulent Natural Convection in a Square Cavity" [1] revealed that, despite simplicity in geometry and boundary conditions, computational predictions with various models showed significant discrepancies between each other and with the experimental results. Based on this experience, two important conclusions can be drawn: first, there is a lack of experimental cavity data suited for validation of turbulence models and numerical computations and, second, the available Reynolds-averaged Navier–Stokes (RANS) turbulence models are not adequate for con-fined buoyancy-driven flows. [2] In the meantime, some improvements in modelling buoyancy-driven flows have been reported, primarily at the level of algebraic stress/flux modelling, see e.g. [2–4]. The study by Dol et al. [2] revealed serious shortcomings of the eddy-diffusivity approach to model buoyancy-driven flows. It also showed that the algebraic stress/flux models fail to reproduce the individual terms in the transport equations in accord with direct numerical simulations (DNS) and that a straightforward analogy with the modelling practice for isothermal turbulent flows and its simple extrapolation to model buoyancy effects fails in many respects. Recently, a systematic term-by-term derivation of a thermal second-moment closure (SMC) model, based on DNS results for turbulent natural convection

---

* Corresponding author.
E-mail address: hanjalic@ws.tn.tudelft.nl (K. Hanjalić).
[1] Present address: National Aerospace Laboratory NLR, P.O. Box 90502, 1006 BM Amsterdam, The Netherlands.

[2] The models presented in [1] include a variety of two equation eddy-viscosity k–ε closures with wall functions, their low-Reynolds-number variants and with some modifications for buoyancy. Also, the application of two differential and several algebraic second-moment models were reported.

Nomenclature

D	depth of cavity
g_i	gravitational acceleration vector $(0, -g, 0)$
H	height of cavity
k	turbulent kinetic energy, $\frac{1}{2}\overline{u_i^2}$
L	width of cavity
l_I	integral length
n_i	wall-normal unit vector
P	pressure
Pr	Prandtl number, ν/α
Ra	Rayleigh number, $g\beta\Delta T H^3 Pr/\nu^2$
Re_t	turbulence Reynolds number, $k^2/(\nu\varepsilon)$
T	temperature
T'	temperature fluctuation
T_{av}	average temperature $(T_{hot} + T_{cold})/2$
T_{cold}	cold-wall temperature
T_{hot}	hot-wall temperature
T_{ref}	reference temperature
t	time
U_i	velocity vector (U, V, W)
U_τ	wall-friction velocity $(\tau_w/\rho)^{1/2}$
u_i	velocity-fluctuation vector (u, v, w)
$\overline{uv}$	turbulent shear stress
V_b	buoyant velocity $(g\beta\Delta T H)^{1/2}$

x_i	Cartesian coordinate vector (x, y, z)
x_n	shortest distance to the nearest wall

Greek symbols

α	thermal diffusivity
β	volumetric thermal expansion coefficient, $1/T_{av}$
ε	dissipation of k
Θ	dimensionless temperature $(T - T_{cold})/\Delta T$, $\Delta T = T_{hot} - T_{cold}$
θ, φ	angles
ν	kinematic viscosity
ρ	mass density
τ_w	wall shear stress, $\rho\nu|\partial U_p/\partial x_n|_w$

Subscripts

b	buoyant
m	mechanical
n	wall-normal
p	wall-parallel
rms	root-mean-square
s	stress
t	turbulent
th	thermal
w	wall value

in a vertical infinite plane channel, was reported by Dol et al. [5]. The simplicity of the geometry and boundary conditions of such a channel flow, which can be computed accurately with standard numerical methods, allowed to focus on details of the turbulence modelling of each term in the transport equations. Further testing of this model should be done in other situations, primarily with heating from below. Although the term-by-term based model of Dol et al. [5] is certainly appealing, for

the computation of complex high Rayleigh number three-dimensional (3D) flows it requires a fine numerical grid in regions adjacent to solid walls and, consequently, significant computational effort.

The aim of the work reported here was to perform full 3D computations with one of the popular low-Reynolds-number k–ε models (KEMs) and with a low-Reynolds-number differential second-moment stress/flux closure, using realistic boundary conditions. Although
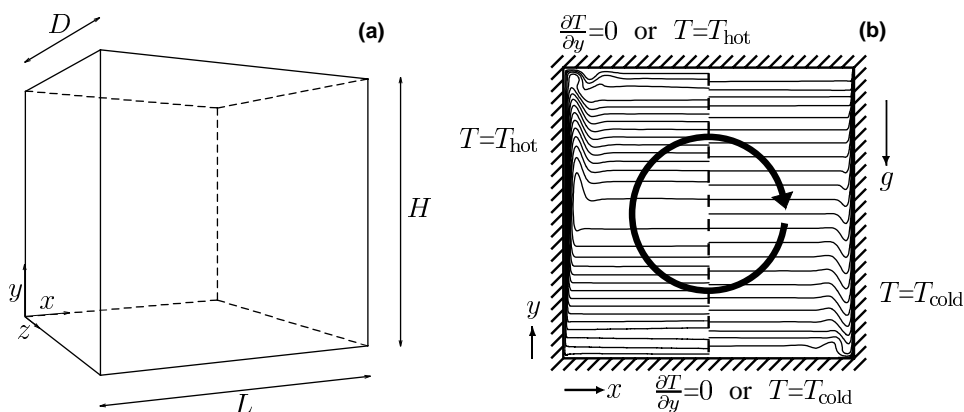

Fig. 1. A schematic picture of the cavity (a) and the plane at $z/D = 0.5$ (b). In the latter, possible thermal boundary conditions and examples of streamlines (left half, circulating clockwise) and isotherms (right half) are depicted.

the models chosen may not be the current 'state-of-the-art', a comparative analysis of the effects captured or ignored by these two distinct classes of models is expected to provide useful information on the model performance for this class of flows and to indicate possible directions for model improvements. The experiments used are those reported by Opstelten [6] and Dol et al. [7] for the side-heated near-cubic enclosure ($H=L=1.5D$) depicted in Fig. 1. As compared with earlier published experimental investigations in similar cavities [8,9], these experiments ensured better two-dimensionality, which reduces the uncertainty in the interpretation of results and makes them suitable for two-dimensional (2D) model validations. The thermal boundary conditions, which are often the origin of deviations between measurements and computation results, are better defined. The Rayleigh number considered, $Ra = 4.9 \times 10^{10}$, was sufficiently high to reduce the importance of the laminar-to-turbulent transition in the downstream corners, which were in focus of our study. The temperature difference was kept sufficiently low to neglect the temperature dependence of fluid properties, eliminating thus any hereto related uncertainty.

The experimental boundary conditions are used to perform 2D and 3D computations for various situations, using the Peeters and Henkes [10] SMC with (and without) the Craft and Launder [11] wall-reflection model and using the Chien [12] KEM, both including low-Reynolds-number and near-wall modifications. The finite-volume numerical computations, with a fine staggered grid and higher-order schemes, ensure confidence in the computational results, enabling thus far a reliable validation of the turbulence models used.

2. Numerical computations

The applied numerical methods and turbulence models are all adopted from existing literature. Hence, we give here only a brief outline of major features of the method used.

2.1. Governing equations and discretization method

The flow considered is described mathematically by the RANS equations, including the averaged energy equation for the mean temperature field that drives the flow by the buoyancy force. The transport equations have been simplified using the Boussinesq approximation, which is valid for fluids with Prandtl numbers close to 1 (for dry air $Pr = 0.71$) and a sufficiently small overheat ratio. The comparison of 2D computational results obtained with and without using the Boussinesq approximation (for details see [1]) shows a negligible difference in the vertical velocity profiles at $y/H = 0.5$ for the present boundary conditions. Applying the

Boussinesq approximation, the Reynolds-averaged equations for mass, momentum and energy conservation reduce to:

$$\frac{\partial U_j}{\partial x_j} = 0, \tag{1}$$

$$\frac{\mathrm{D}U_i}{\mathrm{D}t} = -g_i\beta(T - T_{\mathrm{ref}}) - \frac{1}{\rho}\frac{\partial P}{\partial x_i} + \frac{\partial}{\partial x_j}\left(\nu\frac{\partial U_i}{\partial x_j} - \overline{u_i u_j}\right), \tag{2}$$

$$\frac{\mathrm{D}T}{\mathrm{D}t} = \frac{\partial}{\partial x_j}\left(\alpha\frac{\partial T}{\partial x_j} - \overline{T' u_j}\right). \tag{3}$$

The turbulent stress $\overline{u_i u_j}$ and heat flux $\overline{T' u_j}$ are provided from the turbulence closure models, which are discussed below. The resulting equations are discretized using the finite-volume method. The cavity is 'filled' with a non-uniform rectangular staggered grid with a very fine spacing near the heated vertical walls needed for accurately resolving the steep gradients in the thin buoyancy-driven boundary layers. All variables are calculated straight up to the walls, applying the models with low-Reynolds-number and near-wall modifications. Homogeneous Dirichlet boundary conditions are applied at all walls for all variables, except for the temperature and the pressure, of which the latter does not need any boundary conditions.

Second-order accurate central discretization is used, except for the convection terms, where a second-order accurate bounded upwind scheme is adopted. This bounded upwind scheme belongs to the class of TVD/MUSCL schemes described by Hirsch [13]. For all variables, the upwind scheme is based on the two nearest upstream grid points (known as the linear upwind differencing scheme, LUDS). Van Leer's TVD limiter [14], which keeps the solution locally bounded, is applied to the velocity components and the temperature, while the 'minmod' type (see [13]) is applied to the turbulence variables. As the limiters are non-linear, which is essential for global second-order accuracy, the TVD/MUSCL scheme is implemented in a deferred-correction manner: deviations from the first-order upwind scheme were lumped into the source term. For more details, see [15].

Numerical accuracy was checked by monitoring the variables and residuals during the iteration process (see below) and by refining the grid from 90×60 to 120×80, 150×100 and 180×120 for 2D computations. Unless explicitly stated otherwise, the presented results are always for the finest grid. In case of the 3D computations, the finest grid consisted of $90 \times 60 \times 30$ cells. Consequently, full grid independence is not claimed for the 3D calculations. Nevertheless, useful qualitative information can be obtained by comparing the 3D computation results with the 2D ones obtained on the coarsest grid. When the problem is symmetric

with respect to the centre line at $(x/L, y/H) = (0.5, 0.5)$, which is the case when experimental boundary conditions are not applied, only half of the domain needs to be calculated. For the 3D calculations, the computational domain can be (further) reduced by 50% when the thermal conditions allow symmetry with respect to the plane at $z/D = 0.5$.

2.2. Iteration method

Although the computations performed in this study all aim at a steady solution, a fully implicit first-order time integration is used to obtain this solution, the time marching thus serving as a kind of under-relaxation. Hence, the transient terms are kept in the discretized equations and the computations are started from the best initial guess available (different turbulence model, grid size or Rayleigh number, first-order upwind). The pressure field is solved using the SIMPLE method and a preconditioned conjugate gradient solver applied to the whole domain. All other variables are solved using a line-Gauss–Seidel procedure, sweeping alternatingly in the horizontal direction within z-planes, the latter being traversed forward and backward in the spanwise direction in case of 3D computations. The computations are considered to be converged when the maximum absolute change per iteration of the solution and the maximum absolute finite-volume residuals are below prescribed thresholds. In addition, visualizations of the streamlines, isotherms and other isolines are monitored during the iteration process.

2.3. Turbulence models

The turbulence models used to close the RANS equations in the present work are the low-Reynolds-number KEM of Chien [12] and the SMC of Peeters and Henkes [10].

The KEM of Chien [12] is based on the standard KEM model with low-Reynolds-number and near-wall modifications. The model is similar to the Jones and Launder model, but with damping functions expressed in terms of both the turbulence Reynolds number $Re_t = k^2/(v\varepsilon)$ and wall distance $x_n^+ = x_n U_\tau/v$. The ε equation contains an additional term expressed also as a function of x_n^+. While the use of wall distance seriously limits the application of the Chien model to only regular geometries (the treatment of corners in the present study is already somewhat problematic), its computational robustness offers decisive advantage as compared with physically sounder or more advanced but computationally more demanding models. Another simplification in the present work is the use of the isotropic eddy-diffusivity to provide the turbulent heat flux ('simple gradient-diffusion hypothesis'), i.e., $\overline{T'u_j} = -(v_t/\sigma_T)\partial T/\partial x_j$, which was shown to have serious deficiencies in

capturing the thermal turbulence field both for heating from below and from sides, see e.g., [3,16]. Nevertheless, the Chien model is adopted here because the k–ε computations are only used to illustrate principal differences in performance of the eddy-diffusivity and second-moment modelling approaches.

In the SMC, the modelled transport equations for the turbulent stress $\overline{u_i u_j}$ and heat flux $\overline{T'u_j}$ are solved to close the mean equation set (2) and (3). The model of Peeters and Henkes [10], used in this work, is based on the basic high-Reynolds-number Reynolds-stress model of Gibson and Launder [17] and on the flux model of Launder [18] for forced heat convection in which the buoyancy terms are introduced. In addition to retaining molecular diffusion in all equations, low-Reynolds-number and near-wall effects are introduced by adopting the modifications of the ε equation of Chien [12] and with some additional interventions. The complete model (see Ref. [10]) is summarized in Appendix A, and it will suffice here only to outline its major features:

(i) The stress dissipation tensor ε_{ij} is adopted from [19], with near-wall values expressed in terms of turbulent stress components, wall distance and wall-normal unit vectors.

(ii) The coefficient $c_{\varepsilon 3}$ in the ε equation, associated with the buoyancy production, is evaluated from the expression $c_{\varepsilon 3} = \tanh|\cot(\theta)|$, where $\theta = \angle(U_i, g_i)$ (no summation), leading to $c_{\varepsilon 3} \approx 1$ in the vertical boundary layers, and $c_{\varepsilon 3} \approx 0$ in the horizontal flows, with a smooth transition in between.

(iii) Two versions of the wall-reflection model are considered: the original Gibson and Launder [17] model and the model of Craft and Launder [11]. The latter was originally designed to improve predictions in stagnation regions, as encountered in impinging jets, and is regarded here as a better approach to modelling the flow in cavity corners.

(iv) The nearest wall distance, used in both wall-reflection models, is computed from the harmonic mean of distances from all surrounding walls, integrating the reciprocal of the distance over the space angle ([15], see also Appendix A).

In the following text, the abbreviations SMC-PH will be used for the model of Peeters and Henkes [10] and SMC-CL for the same model but extended with the impinging-jet correction of Craft and Launder [11].

Admittedly, both variants of the SMC model used have a number of deficiencies, to mention the simple linear model for the pressure–strain term with constant coefficients in both the $\overline{u_i u_j}$ and $\overline{T'u_j}$ equations (no low-Reynolds-number and near-wall modifications, except through the inclusion of viscous diffusion and modifications of the ε equation). Despite these simplifications and relatively robust but less exact treatment of the near-wall asymptotic behaviour, the computations with

the SMCs cause much more numerical difficulty than with the KEM. It should also be noted that the full SMC for convective heat transfer entails the solution of 13 differential transport equations for a 2D flow and 17 for a 3D flow, even if only one length-scale-providing equation is considered, here for ε. Besides, the set of SMC equations have to be stabilized using additional source-term relaxation, staggering of the grid points and introduction of a pseudo eddy-viscosity in the mean momentum and energy equations, which are provided from the KEM expressions. For all these reasons, the use of a full SMC for complex industrial 3D buoyancy-driven flows is still not a viable option. For such a purpose, the algebraic models, derived by 'truncation' of differential stress/flux models, seem a better alternative (see e.g., [3,4]). Nevertheless, the computations reported here can serve as useful, though to a certain degree only qualitative, information about the predictive performance of an SMC for a relatively complex 3D flow problem and its comparison with a typical KEM.

3. Results

In presenting the results, a distinction is made between 2D and 3D computations. Although we start with the 2D results, the main focus is on the 3D computations, which are especially interesting for the following reasons:

(i) To the authors' knowledge, these are the first computational results for a side-heated 3D cavity obtained using a fully differential SMC for both the Reynolds stresses and the turbulent heat fluxes, integrated up to the wall.

(ii) The computations are performed using realistic boundary conditions obtained by experiments, eliminating thus far any ambiguity related to possible mismatching of the computational boundary conditions.

(iii) The confirmed validity of the Boussinesq approximation eliminates any doubt that a possible departure from it may have caused a discrepancy between the Boussinesq-based computations and the measurements.

(iv) The availability of measured boundary and field data allows to detect true effects of thermal and mechanical three-dimensionality and to judge the ability of the KEM and the SMC to reproduce these effects.

3.1. Two-dimensional computations

The application of adiabatic conditions at the horizontal walls has been customary in studies of side-heated natural convection for a long time. Such a configuration was expected to minimize the thermal influence of the horizontal walls on the flow, giving full attention to the vertical boundary layers. 2D computations for such an adiabatic configuration (with isothermal vertical walls and adiabatic horizontal ones) for $Ra = 5 \times 10^{10}$ were reported earlier by Dol et al. [20]. These 2D results were compared with experimental data available at that time, obtained with insulated lateral walls (passive case, see next section). The adiabatic results for isotherms and streamlines are shown in Fig. 2 by solid lines. The differences between the KEM and the SMC for the velocity and temperature appeared to be quite large in the corner regions, where the vertical boundary layers impinge on the horizontal walls. The DNS data of Janssen [21] and the experiments of Opstelten [6] supported qualitatively the SMC computational results. The impinging boundary layers carry in their outer regions the entrained fluid that is colder than the local fluid in the upper left corner and warmer than the fluid in the bottom right corner, causing in both regions notable reverse flow loops and subsequent monotonic or oscillatory recovery. A small recirculation bubble, attached to the horizontal wall downstream from the corner loop was detected in each corner. Detail plots also depicted another, even smaller bubble, trapped in each loop. This phenomenon, accompanied with strong streamline curvature, was, on the whole, better captured by the SMC than by the KEM.

The SMC-CL impinging-jet correction damped somewhat the strength of the streamline loops, but still much stronger flow reversal and weaker stratification was predicted by the SMC-CL than by the KEM. The velocity profiles computed for adiabatic horizontal walls at $y/H = 0.9$ and $x/L = 0.1$ (positions marked by dots in Figs. 2(d)–(f)) were compared with the experimental data in Figs. 3 and 4 (passive case only). Fig. 4(b) shows that the SMC-CL impinging-jet correction decreases the normal stress perpendicular to the horizontal wall. The correction, which is still small at $y/H = 0.9$, improves the prediction of the velocity profile, as can be seen from Fig. 3(a) for the horizontal component on which the effect is most felt. Just downstream of the impingement at $x/L = 0.1$ (see Figs. 3(b) and 4(a)), the differences between the models are more pronounced owing to a different prediction of position and size of the attached recirculation bubble. It is no longer clear whether the impinging-jet correction improves the results, but one can say that the SMC results are in better overall (qualitative) agreement with the experiments than the KEM.

However, the computation results for *isothermal* horizontal walls, which corresponds to the experimental conditions, show that the effect of these boundary conditions on the flow structure is rather large for the SMCs, as is clearly shown by the other lines in Figs. 2–4. The isotherms and streamlines predicted by the SMCs are now almost equal to the KEM results, which means a large stratification near the horizontal walls and
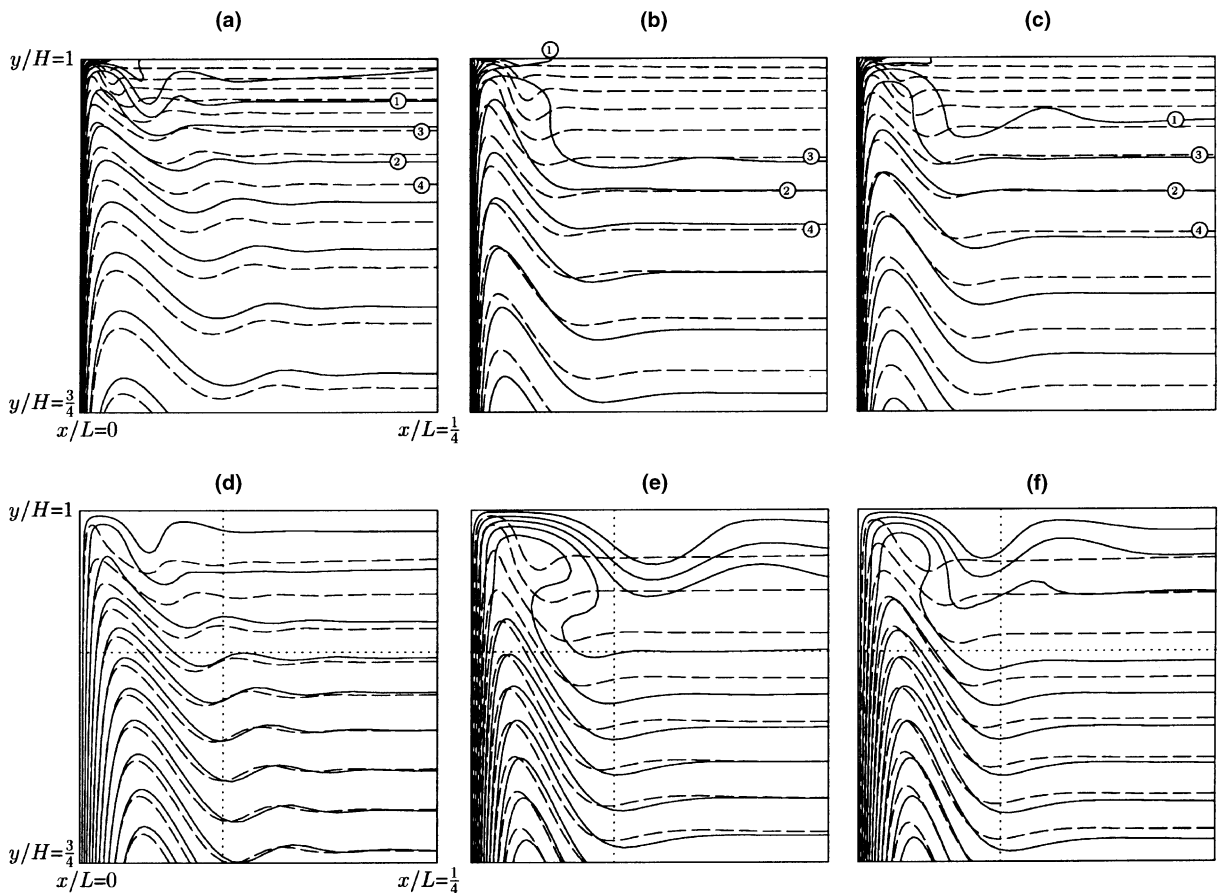
Fig. 2. Isotherms (a–c) and streamlines (d–f) in the left-upper quarter of the cavity with adiabatic (– , 1: $\Theta = 0.82$, 2: $\Theta = 0.76$) and isothermal (– –, 3: $\Theta = 0.82$, 4: $\Theta = 0.76$) horizontal walls. The results are obtained by 2D computations applying the KEM (a,d), SMC-PH (b,e) and SMC-CL (c,f). The pitch between the isotherms is fixed at $\Delta\Theta = 0.03$. The dots in (d–f) mark the positions $x/L = 0.1$ and $y/H = 0.9$.

consequently only little recirculation due to damped turbulence levels and reduced entrainment in the vertical boundary layers. The conclusions drawn from the comparison between the experiments and the computations for the *adiabatic* horizontal walls do not apply anymore. In the sequel on the 3D results it will be made plausible that the differences between the 2D computation results (isothermal horizontal walls) and the experimental data are caused by 3D effects. The resemblance of the adiabatic 2D computation results with the experiments is fortuitous and the added value of the SMCs is not as small as might be concluded from the isothermal 2D computation results.

3.2. Three-dimensional computations

The availability of the measured thermal boundary conditions at all walls makes it possible to extend the computations from 2D to 3D. This requires a large computational effort: the 3D computations converge

very slowly because of some oscillations in the core region, which do not have a large impact on the prediction of the flow in the boundary layers and corners. Therefore, the convergence criterion is relaxed for the 3D computations.

A selection of results will be shown for two types of thermal boundary conditions at the lateral walls, corresponding to two different experimental approximations of adiabatic conditions by Opstelten [6] and Dol et al. [7]: (1) application of (imperfect) insulation, and (2) imposing a temperature distribution corresponding to a stratified wall heating minimizing uncontrolled heat losses and thus improving flow two-dimensionality. The first situation is referred to as the *passive case* and the second as the *active case*. For both situations, the measured wall-temperature profiles have been applied in the computations. Furthermore, computations have also been performed with perfect adiabatic boundary conditions at the lateral walls, which is referred to as the *adiabatic case*. All computation results shown in this
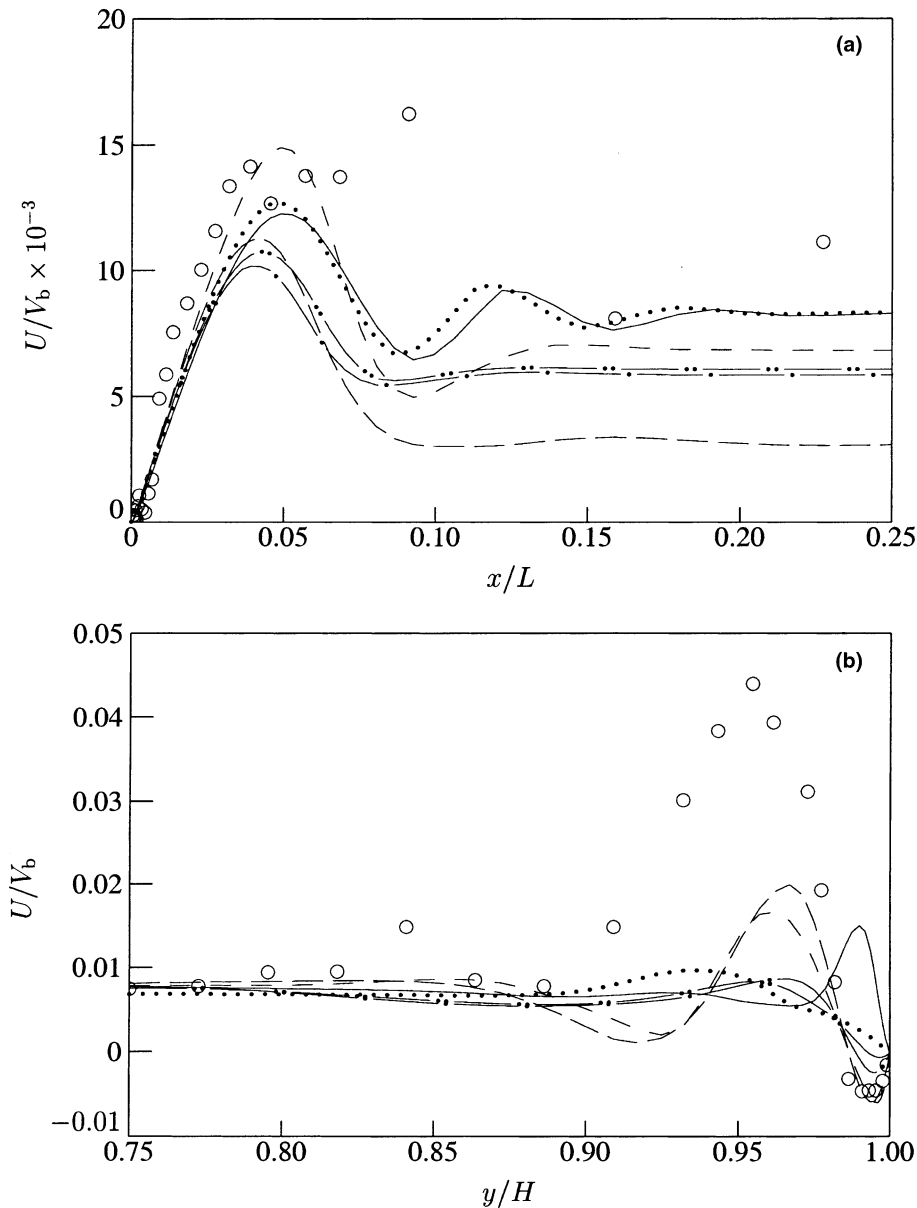
Fig. 3. The horizontal velocity U/V_b at $y/H = 0.9$ (a) and $x/L = 0.1$ (b). The symbols ($\circ$) are measurements at $z/D = 0.5$ for the passive case and the lines are 2D computational results for adiabatic ($\cdots$ = KEM, $--$ = SMC-PH, $-\cdot-$ = SMC-CL) and isothermal horizontal walls ($-$ = KEM, $-\cdot-$ = SMC-PH, $-\cdot\cdot-$ = SMC-CL).

section are for isothermal horizontal and vertical (side) walls.

Although different wall conditions generated somewhat different flow patterns close to the lateral walls, we focus here, for brevity, only on the midplane at $z/D = 0.5$. Specific attention was given to the corner flow and the vertical boundary layers, of which the latter have traditionally been in focus of earlier literature on natural-convection cavity flows. More details can be found in [15].

3.2.1. The corner flow

In order to investigate whether 3D effects are responsible for the large deviations between 2D computation results and the experimental data obtained for the passive case, Figs. 2–4 are replotted with superimposed 2D and 3D results (in the mid-plane) enabling a direct comparison, see Figs. 5–8. In Figs. 5 and 6, the left half shows KEM results, while the right half shows SMC-CL results. In the upper half, 2D computation results are compared with 3D computation results for the passive
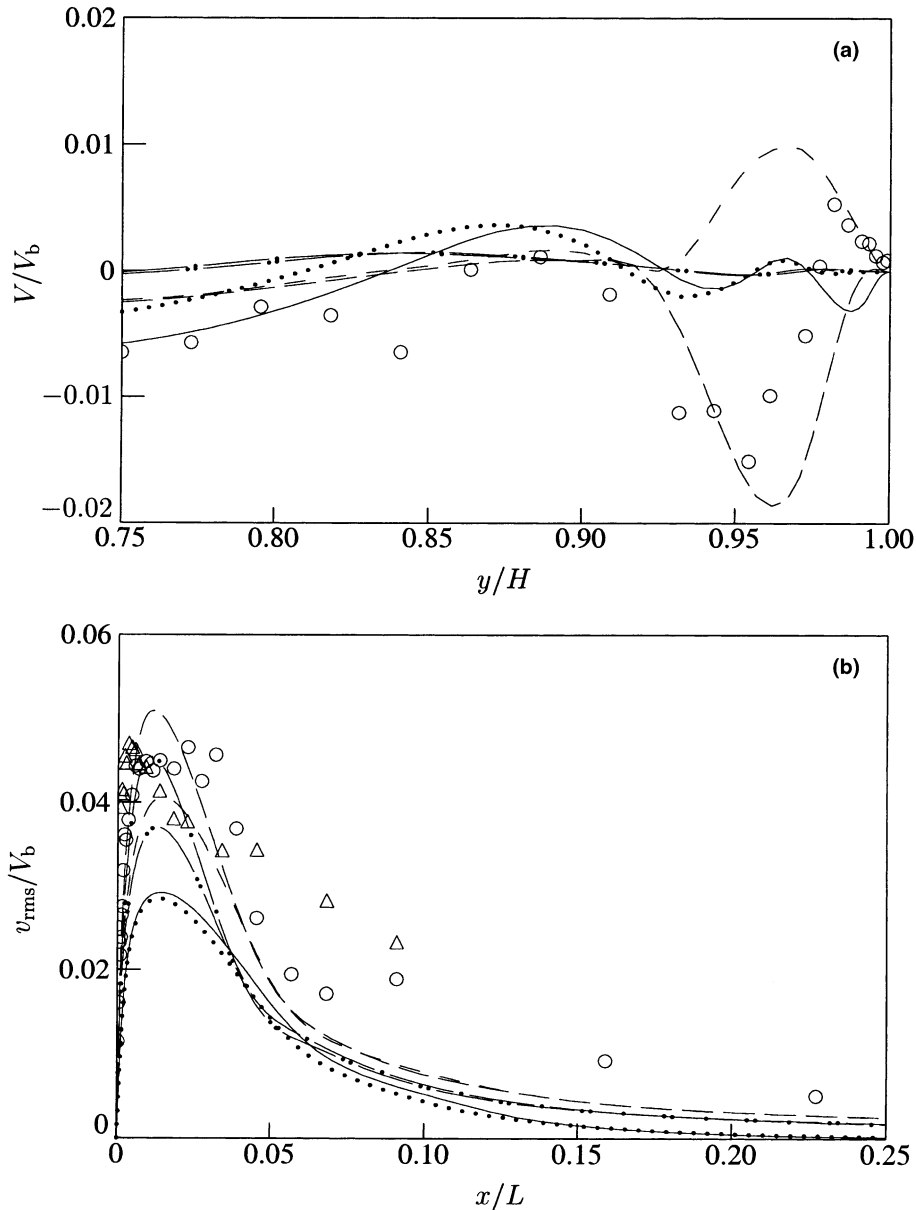
Fig. 4. The vertical velocity V/V_b at $x/L = 0.1$ (a) and its rms fluctuation v_{rms}/V_b at $y/H = 0.9$ (b). The symbols are measurements at $z/D = 0.5$ ($\circ$ = passive, $\triangle$ = active case) and the lines are 2D computational results for adiabatic ($\cdots$ = KEM, $--$ = SMC-PH, $--$ = SMC-CL) and isothermal horizontal walls ($-$ = KEM, $-\cdot-$ = SMC-PH, $-\cdot\cdot-$ = SMC-CL).

case. In the lower half, 3D computation results for the active and adiabatic case are compared. Since all the 3D computations have been performed on a $90 \times 60 \times 30$ grid, the 2D results presented here are for the 90×60 grid to enable comparisons with the same numerical resolution.

Fig. 5 shows that moving in sequence from the passive to the active, adiabatic and 2D case, the isotherms in the left-upper quarter of the mid-depth plane of the cavity become less curved, with the largest jump between passive and active, whereas the difference between the adiabatic and 2D case remains relatively small. Apparently, an increase of heat losses through the lateral walls tends to increase the curvature of the isotherms, while the presence of the lateral walls itself is of minor influence in the mid-plane. Consequently, it can be concluded that the 3D effect has a thermal nature (heat losses) and not a mechanical one (friction). A further observation
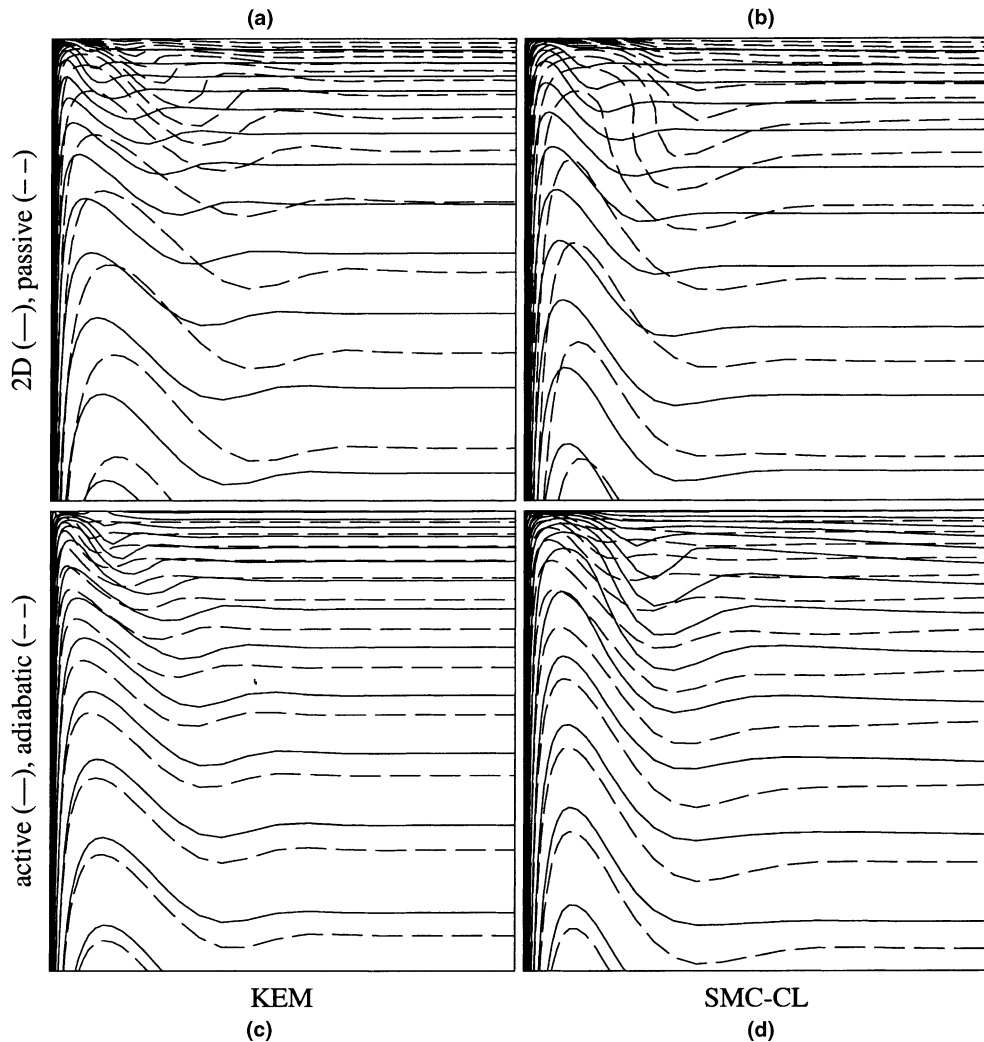
(a) (b)

KEM SMC-CL
(c) (d)

Fig. 5. Isotherms in the left-upper quarter of the 2D cavity and of the 3D cavity's midplane ($z/D = 0.5$). The results are obtained by 2D computations applying the KEM (a: $-$) and SMC-CL (b: $-$), and 3D computations applying the KEM (a: $--$ = passive, c: $-$ = active, $--$ = adiabatic case) and SMC-CL (b: $--$ = passive, d: $-$ = active, $--$ = adiabatic case).

that can be made from Fig. 5 is that the differences between the KEM and the SMC(-CL), which are small for the 2D results, also increase with the heat losses. As expected, the SMC predicts stronger curvature than the KEM.

The influence of the thermal 3D effect on the streamlines is depicted in Fig. 6. The streamlines for the SMC-CL in the passive case show the same kind of corner structure as was obtained with 2D computations applying adiabatic boundary conditions at the horizontal walls. On the other hand, the stratification near the top wall (see Fig. 5) is very large for the passive case, whereas it was small for the adiabatic 2D computations. It can be concluded that the destabilizing effect of the

heat losses is stronger than the stabilizing effect of the stratification.

Figs. 7 and 8 validate the corner flow structure as predicted by the SMC-CL in the passive case by comparing the results with the corresponding measurements and with the other computation results. The SMC-CL predicts the 3D corner flow better than the KEM does. In general, the 3D computations for the passive case yield higher values of velocity components and their second moments than for the active-case and 2D computations and hence they are in better agreement with the measurements in that respect. Again, similarity is observed with the 2D results for adiabatic horizontal walls, shown in Figs. 3 and 4.
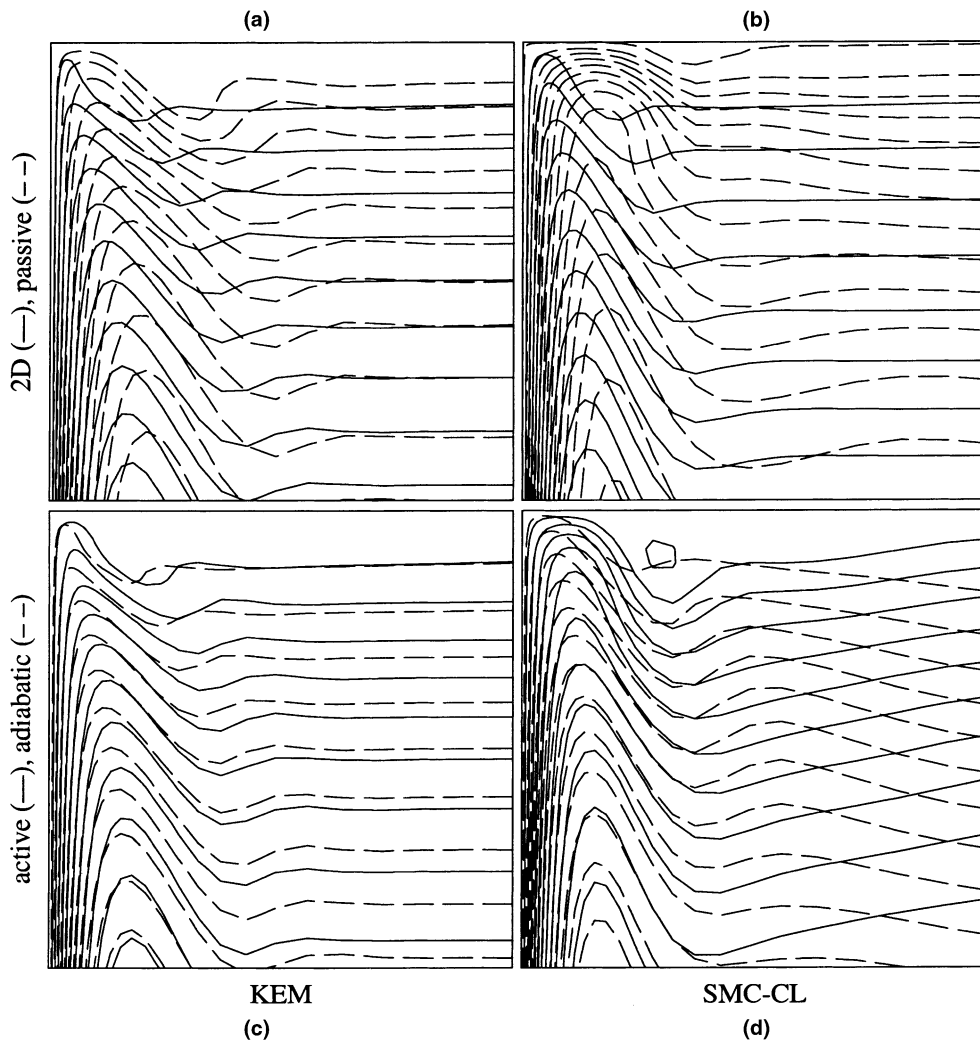
Fig. 6. Streamlines in the left-upper quarter of the 2D cavity and of the 3D cavity's midplane ($z/D = 0.5$). The results are obtained by computations, see the caption of Fig. 5 for an explanation of the line types.

Comparison of the 2D computation results in Figs. 3,4,7 and 8 (isothermal horizontal walls) illustrates the effect of grid refinement from 90×60 to 180×120 (see also Figs. 2, 5 and 6). Even at $y/H = 0.9$, the coarse grid results are still quite accurate. However, the differences are more pronounced at $x/L = 0.1$, owing to the streamline curvature which requires fine grids for accurate solutions. Further downstream, e.g., at $x/L = 0.3$, the coarse grid is sufficient, just as for the vertical boundary layers and the core region.

In the horizontal boundary layers, far enough downstream for the turbulence intensity to become small, the differences between the KEM and SMC-CL results are mainly due to convection of upstream differences and are small compared to the 3D effect. Fig. 9 shows the horizontal velocity along the top wall at

$x/L = 0.3$ and $x/L = 0.5$. The 3D computational results are closer to the measurements than the 2D ones, but the 3D results are still much smoother (i.e., more turbulent) compared to the measurements, which exhibit notable oscillations when approaching the wall.

Fig. 10 shows that, more than the velocity components themselves (see Figs. 7(b) and 8(a)), the profiles for their root-mean-square (rms) fluctuations at $x/L = 0.1$ look reasonably similar for the KEM and the SMC-CL. This is surprising in view of the known inadequacy of the KEM for predicting turbulent normal stresses and is probably due to the relatively low level of turbulence in these cross-sections. When compared with the measurements for the passive case, the turbulence level for $y/H < 0.9$ is better predicted by the 3D computations than by the 2D computations, which predict a
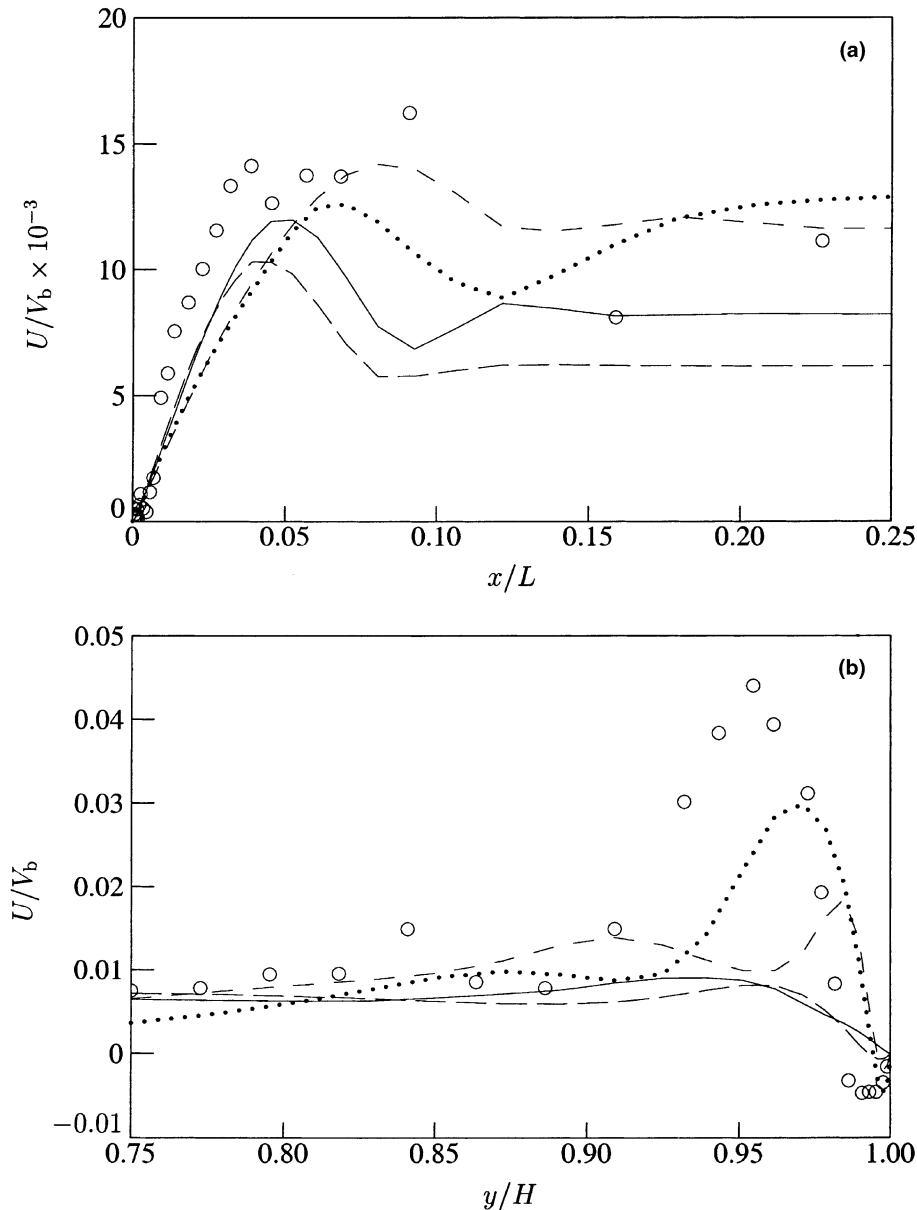
Fig. 7. The horizontal velocity U/V_b at $y/H = 0.9$ (a) and $x/L = 0.1$ (b). The symbols (○) are measurements at $z/D = 0.5$ for the passive case and the lines are 2D computational results for isothermal horizontal walls (— = KEM, – – = SMC-CL) and 3D computations for the passive case (- - = KEM, ⋯ = SMC-CL).

lower level. However, even the 3D computations are unable to capture the sharp near-wall peaks at $y/H > 0.9$, consistent with the prediction of the velocity components.

3.2.2. The vertical boundary layers

The vertical boundary layers act as the driving force of the flow and their proper simulation is crucial for accurate prediction of the rest of the flow downstream

(corner, horizontal boundary layer) and in the cavity core region. The vertical boundary layers have received a lot of attention in the literature, both along semi-infinite plates [10,22,23], and in cavities (e.g., [8]). Fluid velocity develops a wall-jet like profile with a peak very close to the wall, which needs to be resolved. Adequate wall functions are not available and very fine grids are thus needed in the near-wall region. From a modeller's point-of-view, the major problem related to the vertical
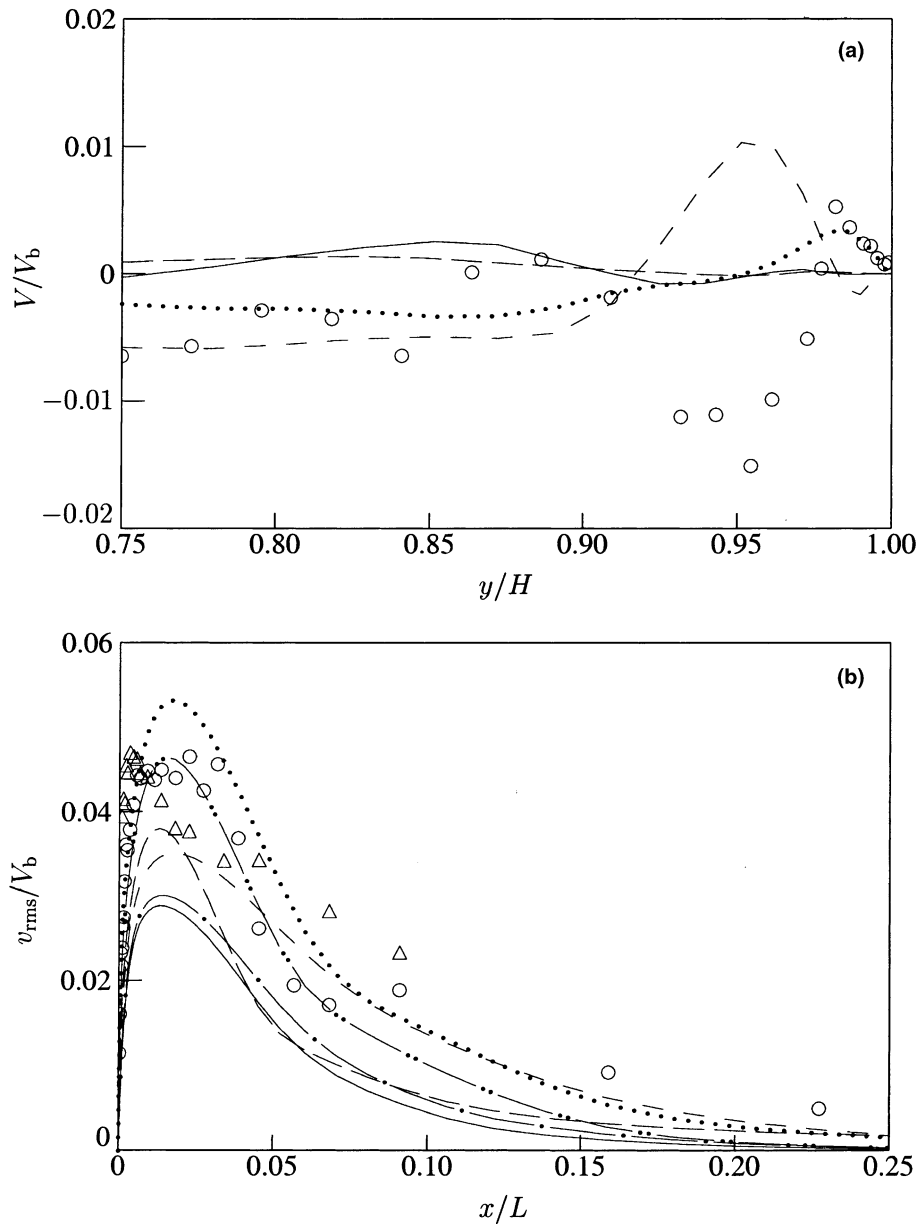
Fig. 8. The vertical velocity V/V_b at $x/L = 0.1$ (a) and its rms fluctuation v_{rms}/V_b at $y/H = 0.9$ (b). The symbols are measurements at $z/D = 0.5$ ($\circ$ = passive, $\triangle$ = active case) and the lines are 2D computational results for isothermal horizontal walls ($-$ = KEM, $--$ = SMC-CL) and 3D computations for the passive (- - = KEM, $\cdots$ = SMC-CL) and active case ($-\cdot-$ = KEM, $-\cdot\cdot-$ = SMC-CL, only for those cases for which measurements are available).

boundary layers is the laminar-to-turbulent transition. Predicting laminar-to-turbulent transition is a challenge for any turbulence model, particularly in external (buoyant or non-buoyant) boundary layers, when the transition occurs by natural instability and less by turbulence entrainment from the outer flow. Unlike on an infinite plate, where the incoming flow can be fully laminar, even at moderate Rayleigh numbers in en-

closures the circulating fluid always convects some disturbances and remnants of upstream decaying turbulence, despite possible laminarization along horizontal walls. Hence, the transition in enclosures is usually associated with a revival of weak background turbulence when the conditions are favourable (sufficiently strong buoyancy and strain rate). In this respect, the transition in enclosures is less uncertain and
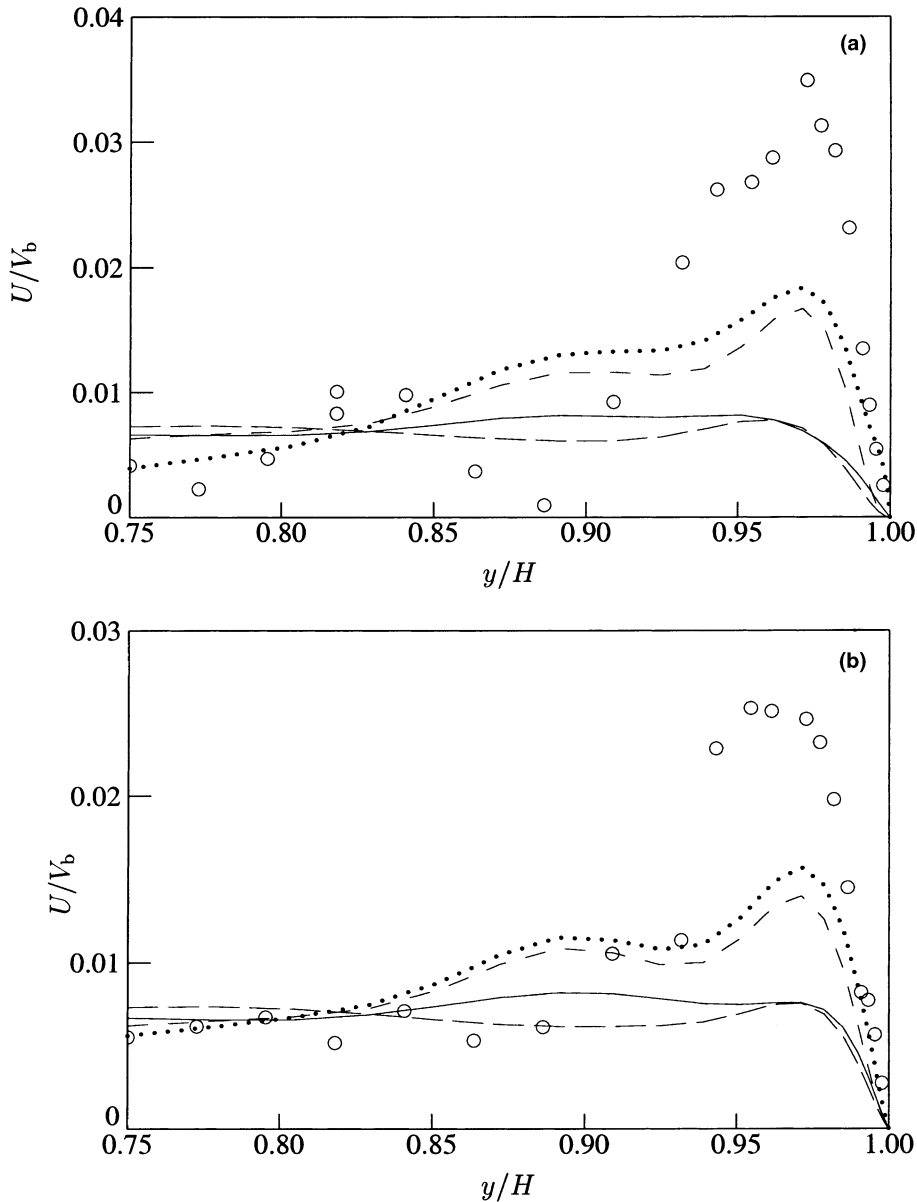
Fig. 9. The horizontal velocity U/V_b at $x/L = 0.3$ (a) and $x/L = 0.5$ (b). The symbols (○) are measurements for the passive case at $z/D = 0.5$ and the lines are 2D computational results for isothermal horizontal walls (— = KEM, – – = SMC-CL) and 3D computations for the passive case (- - = KEM, ··· = SMC-CL).

more suitable for validating the transition performance of a model. Nevertheless, most models with low-Reynolds-number modifications that perform reasonably well for transitional *forced* convection, predict a too late transition in *natural*-convection boundary layers. Some other models are more successful, see e.g., [4]. A not very elegant but effective remedy is the use of artificial triggering by injecting a sufficient amount of turbulent energy into the laminar boundary layer at a

given point in the upstream part of the developing vertical boundary layer.

Figs. 11 and 12 show the vertical velocity at several heights in the hot vertical boundary layer. First, in Fig. 11, the profiles in the laminar and transitional part of the boundary layers are shown. At those locations, the differences between the computational results with different models and for different boundary conditions are small owing to the low turbulence intensity, short
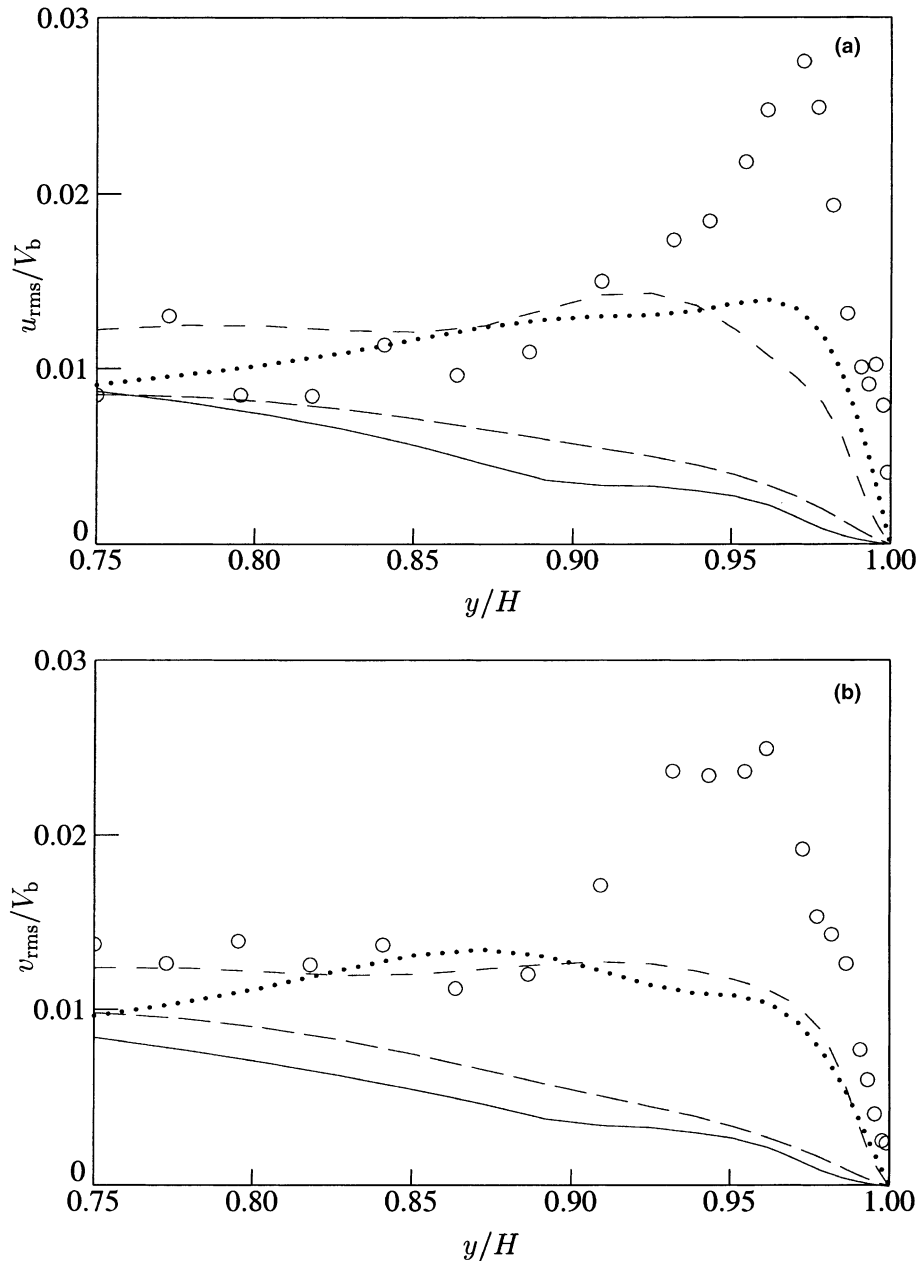
Fig. 10. The horizontal (a) and vertical (b) components of the rms velocity fluctuation $u_{i,\mathrm{rms}}/V_{\mathrm{b}}$ at $x/L = 0.1$. For an explanation of the symbols and line types, see the caption of Fig. 9.

development track and relatively little (accumulated) influence of the lateral-wall boundary conditions. The same applies to the measured results. The main differences appear between the computations and the measurements. The numerical models are all able to predict the fully laminar (Fig. 11(a)) and fully turbulent (Fig. 11(c)) boundary layer reasonably well, but are incapable to predict the transition from laminar to turbulent in accordance with the experimental data (see Fig. 11(b)).

For the hot boundary layer, the measurements indicate a quick transition somewhere between $y/H = 0.3$ and $y/H = 0.5$, whereas the transition trajectory obtained by the computations is longer, as it starts already around $y/H = 0.1$.

Since we focused only on the fully turbulent region, the local triggering suggested by Henkes [24] is used here, providing fixed profiles for the turbulent kinetic energy and its dissipation rate in the areas
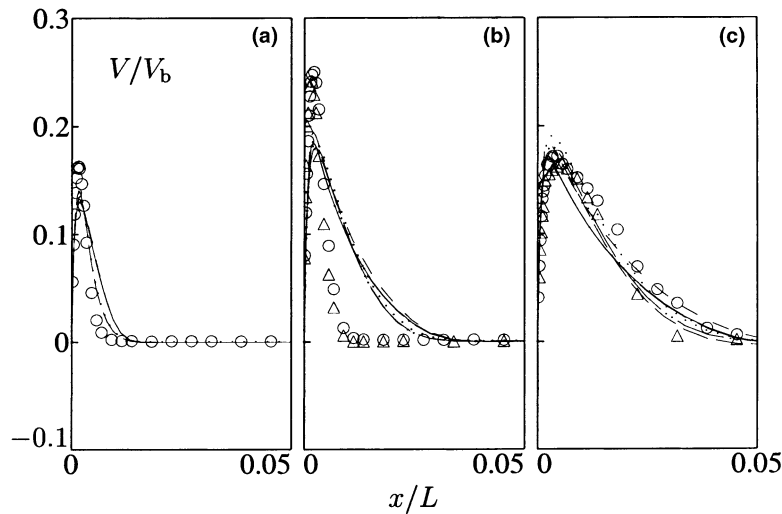
Fig. 11. The vertical velocity V/V_b at $y/H = 0.1$ (a), $y/H = 0.3$ (b) and $y/H = 0.5$ (c). The symbols are measurements at $z/D = 0.5$ ($\circ$ = passive, $\triangle$ = active case) and the lines are 2D computational results for isothermal horizontal walls (– = KEM, – – = SMC-CL) and 3D computations for the passive (- - = KEM, $\cdots$ = SMC-CL) and active case (–·– = KEM, –··– = SMC-CL).

$(x/L < 0.15, y/H < 0.15)$ and $(x/L > 0.85, y/H > 0.85)$. Without this triggering the numerical transition would have been delayed until as far as $y/H = 0.7$ along the hot-wall. The chosen triggering method ensures a fully turbulent boundary layer at $y/H = 0.5$. Fig. 12 shows in more detail the profiles at the more downstream locations in the hot boundary layer, where both the computations and measurements are now fully turbulent. Fig. 12 shows that the differences between the measurements for the passive and the active case are reproduced by the computations. The 2D computation results are in reasonably good agreement with the measurements (and computations) for the active case. The excellent matching of the 3D SMC-CL computation results for the passive case at $y/H = 0.9$ ensures that optimal starting conditions are provided for the corner flow, in order to make a comparison between computations and experiments worthwhile.

The experimental data for the vertical velocity in the hot vertical boundary layer at height $y/H = 0.7$ are shown for the passive (Fig. 13(a)) and the active (Fig. 13(b)) case. Also shown are lines that represent the velocity profiles predicted by 2D and 3D KEM computations at the same location. The computed profiles at height $y/H = 0.3$ in the cold vertical boundary layer are added after reflecting them with respect to the centre of the cavity. It can be observed that in the active case all computational results coincide and agree quite well with the measurements, especially for the maximum velocity close to the wall. This means that there is a high degree of two-dimensionality, obtained by the thermally controlled lateral walls. Consequently, the measurements for the active case are suitable for validation of 2D

computations of the flow considered. Practical details are given in [7].

The asymmetry caused by the heat losses through the insulated lateral walls in the passive case is captured well by the 3D computations. Surprisingly, the reflected 3D results coincide with the results from the 2D computations. This means that the flow downwards the passively heated lateral walls (see [7]) does not slow down the downward flow in the cold vertical boundary layer. The additional flow along the lateral walls is counter-balanced purely by an increase in the upward flow by more than 50% in the hot vertical boundary layer. Hence, the effect of heat losses through the insulation of the lateral walls is a significant enhancement of the flow velocity in the hot vertical boundary layer and, consequently, stronger impingement and streamline curvature in the left-upper corner. However, a convincing explanation for this preference is lacking, since the decreased core temperature leads to an increase of the local Rayleigh number in the hot vertical boundary layer and to a decrease on the opposite cold-wall. Confusingly, the numerical results published by Ince and Launder [25] show that the effect of three-dimensionality is mainly a *reduction* of the vertical velocity along the cold-wall. These authors accounted for heat losses through the lateral walls by using experimental wall-heat-transfer relations.

Figs. 14 and 15 show the rms of the velocity fluctuations in the hot vertical boundary layer at $y/H = 0.5$ and $y/H = 0.7$. The higher the location, the more developed the boundary layer becomes, and the larger is the separation between the passive case and the active case for both the measurements and the computations. Of course, the turbulence level is largest for the passive
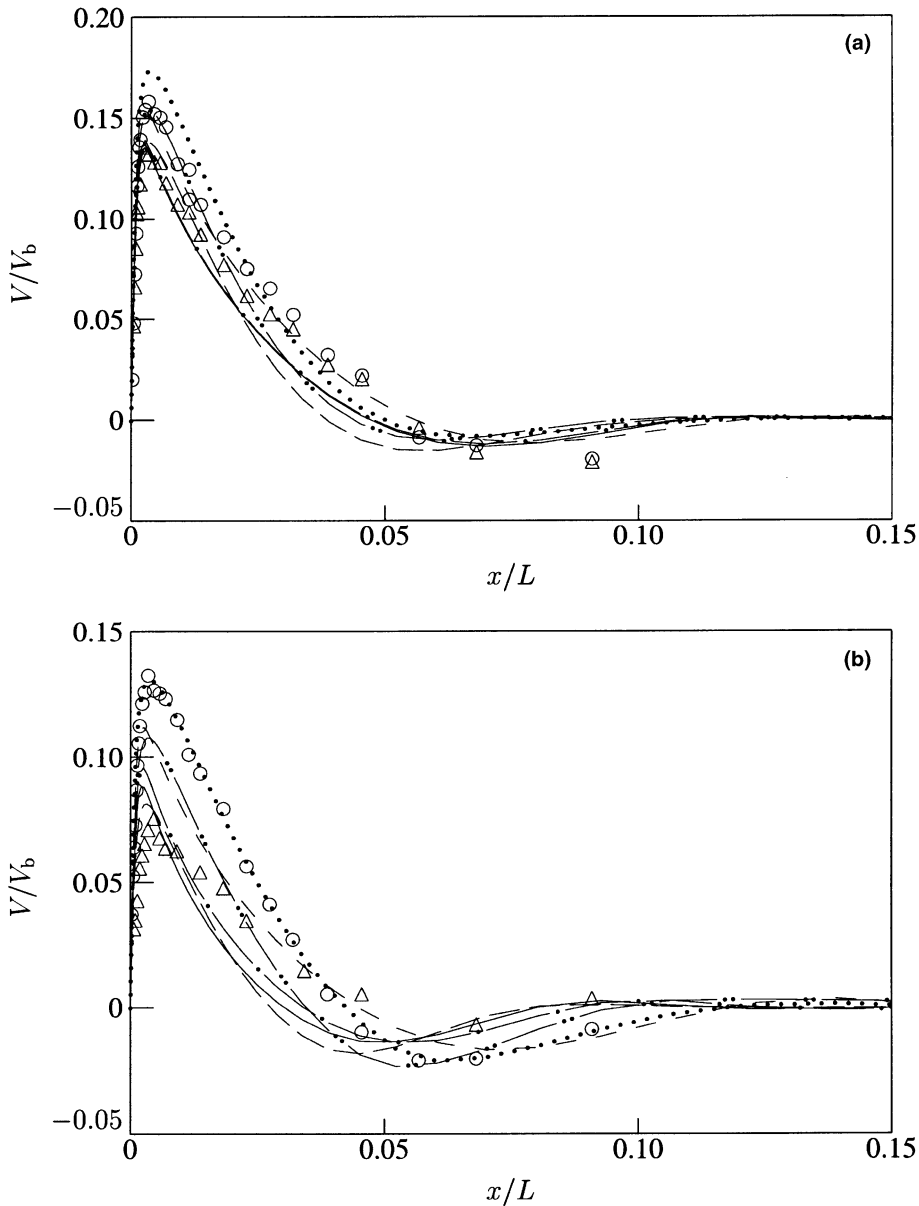
Fig. 12. The vertical velocity V/V_b at $y/H = 0.7$ (a) and $y/H = 0.9$ (b). For an explanation of the symbols and line types, see the caption of Fig. 11.

case, caused by the increased flow velocity, as reported above. The 2D results coincide with the 3D results for the active case almost everywhere, except at the outer edge of the boundary layer, where the 2D SMC-CL results yield larger normal stresses, especially at $y/H = 0.7$.

It is well-known that, unlike SMCs, k–ε models are unable to cope with turbulence anisotropy, leading to unrealistically similar components of the normal stress at the same location. Paradoxically, this would have

been beneficial at $y/H = 0.5$, although the level predicted by the KEM is too low. The SMC-CL predicts the vertical component at this height quite well, except for the peak very close to the wall that is measured for both the passive and active configuration and that is supported by 2D DNS of Janssen [21]. Unfortunately, the strong anisotropy predicted by the SMC-CL leads to a much too low level for the horizontal component. The experimental values of u_{rms} at $y/H = 0.5$, on the other hand, are probably too large due to slow oscil-

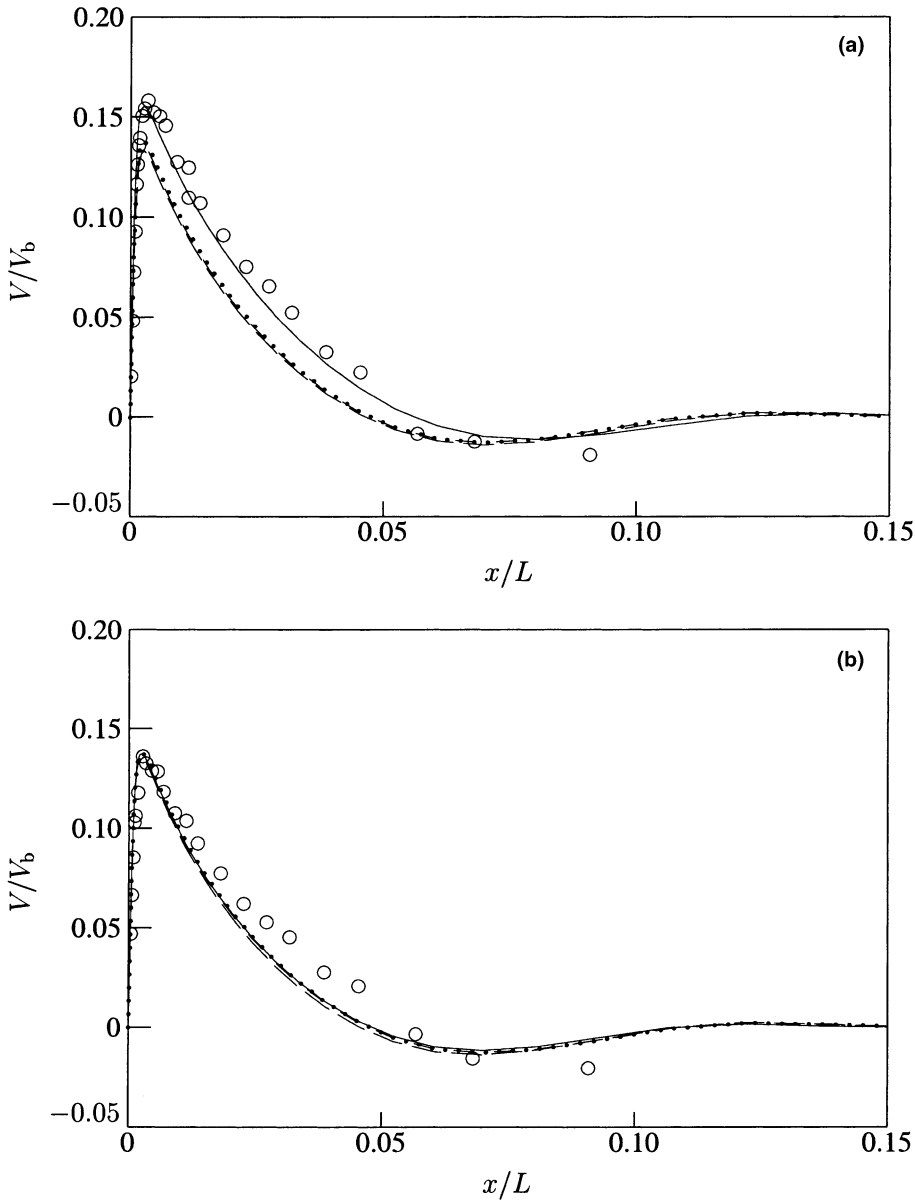Fig. 13. The vertical velocity V/V_b at $y/H = 0.7$ for the passive (a) and active case (b). The symbols (○) are measurements and the lines are 2D ($\cdots$) and 3D ($-$, $z/D = 0.5$) KEM computations ($- \cdot$ = 2D data and $- -$ = 3D data at $y/H = 0.3$, reflected with respect to the centre of the cavity).

lations of the horizontal velocity that have been observed at that location during the measurements. At $y/H = 0.7$, the experimental results indicate significant anisotropy, but the SMC–CL still yields strong overpredictions, resulting in an overshoot for the vertical component, whereas the horizontal component is predicted satisfactory.

Fig. 16 shows the turbulent shear stress in the hot vertical boundary layer. At $y/H = 0.5$, the computations

underpredict the experimental results, but as mentioned above, the experimental correlations at this location containing the horizontal velocity fluctuation u are probably too large. At $y/H = 0.7$, the situation is opposite, although the discrepancy is less serious and the differences between the measurements for the passive and active case are predicted qualitatively correct. The 2D results are again close to the active 3D results. At $y/H = 0.9$, the shear stress is predicted very well by the
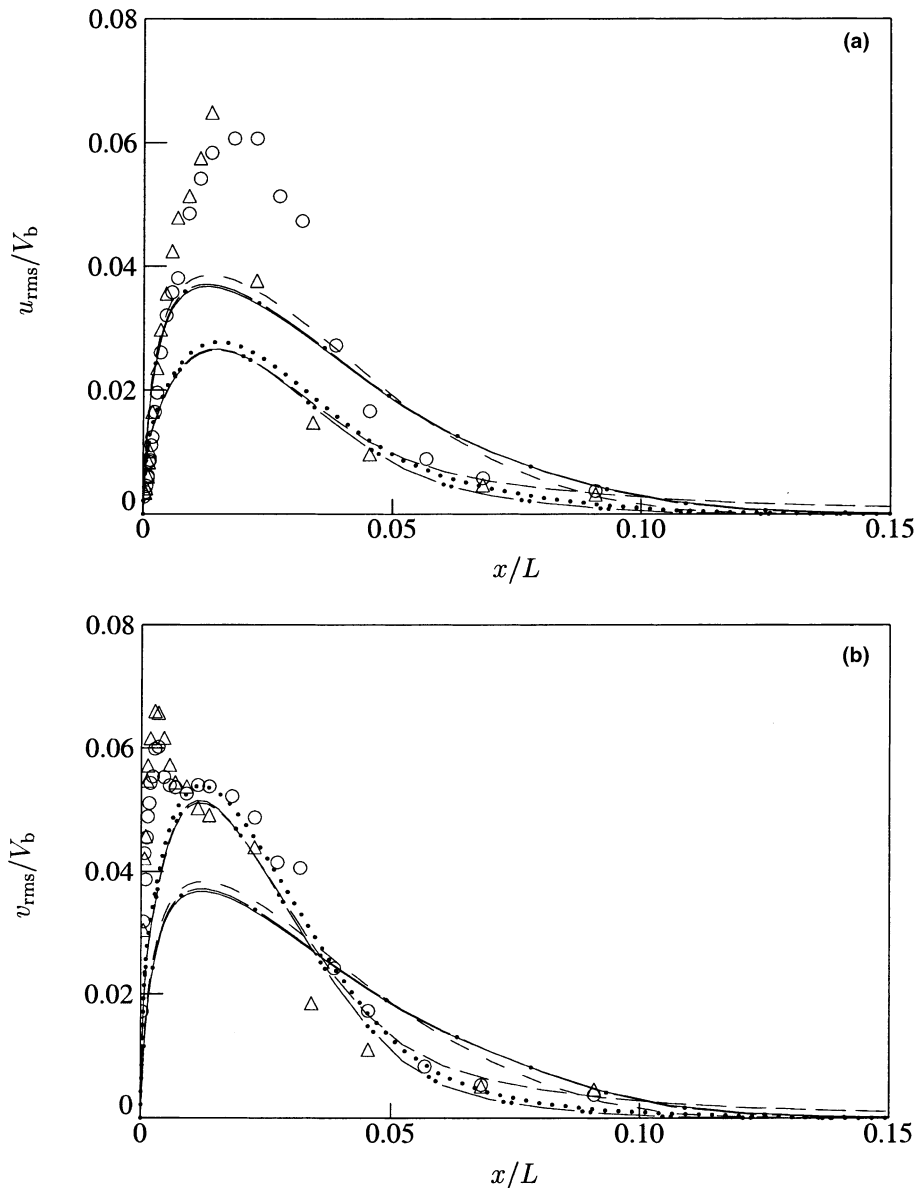
Fig. 14. The horizontal (a) and vertical (b) components of the rms velocity fluctuation $u_{i,\mathrm{rms}}/V_\mathrm{b}$ at $y/H = 0.5$. The symbols are measurements at $z/D = 0.5$ ($\circ$ = passive, $\triangle$ = active case) and the lines are 2D computational results for isothermal horizontal walls ($-$ = KEM, $--$ = SMC-CL) and 3D computations for the passive ($\cdot\text{-}\cdot$ = KEM, $\cdots$ = SMC-CL) and active case ($-\cdot-$ = KEM, $-\cdot\cdot-$ = SMC-CL).

3D computations, whereas the 2D computations underpredict the turbulence level.

4. Conclusions

The computational study of turbulent natural convection in a near-cubic cavity with differentially heated isothermal side walls provides useful and novel infor-

mation on the flow pattern and turbulence characteristics in this generic type of buoyancy-driven internal flow for several sets of boundary conditions. Considered are two types of horizontal walls, adiabatic and isothermal (cold bottom and hot top wall), and two types of lateral walls, imperfectly insulated (passive case) and nearly adiabatic (active case). The latter type is realized with stratified wall heating by which heat losses are compensated to ensure a near-2D thermal situation. An
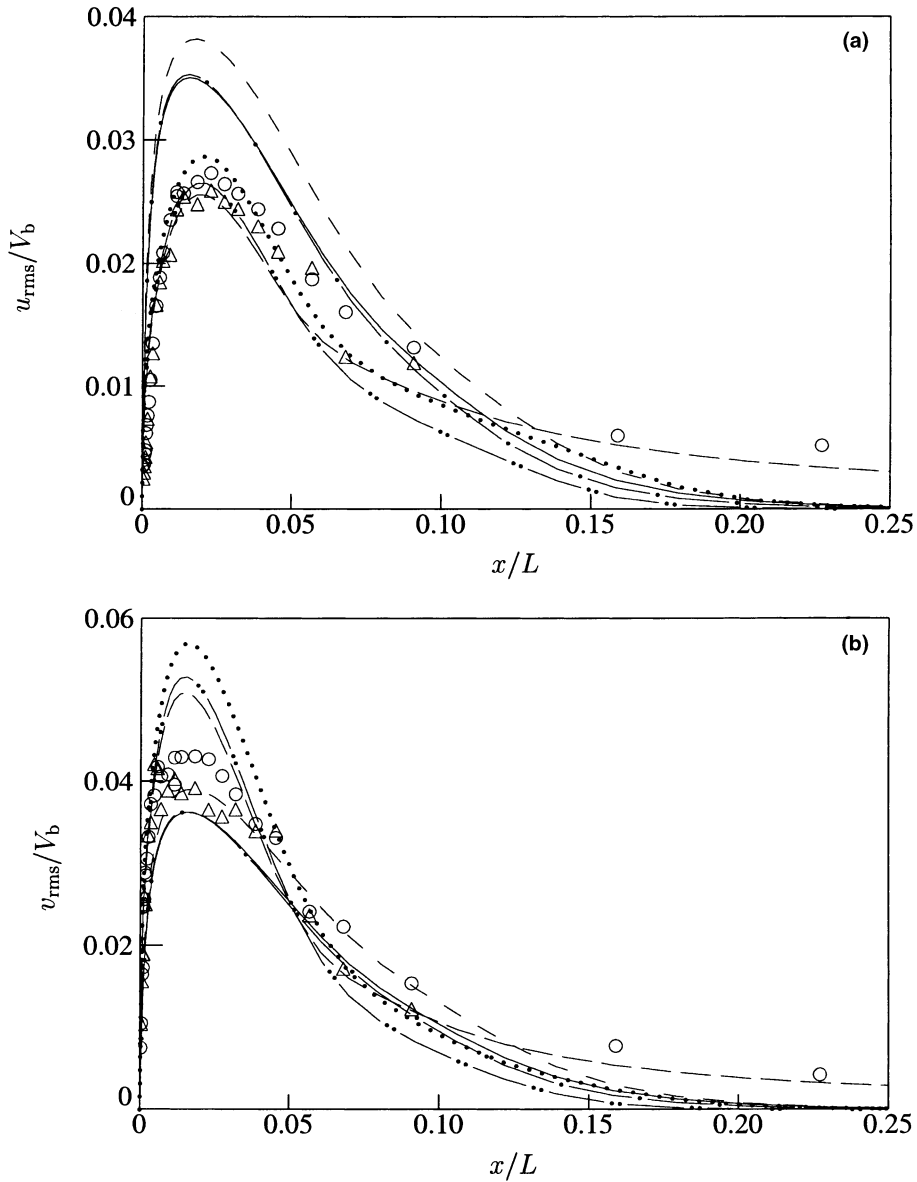
Fig. 15. The horizontal (a) and vertical (b) components of the rms velocity fluctuation $u_{i,\mathrm{rms}}/V_{\mathrm{b}}$ at $y/H = 0.7$. For an explanation of the symbols and line types, see the caption of Fig. 14.

SMC and a KEM, both with low-Reynolds-number modifications, are used for 2D and 3D numerical computations of the flow. The following conclusions are drawn:

1. The 3D computations with the KEM of Chien [12] and with the SMC of Peeters and Henkes [10], both with low-Reynolds-number modifications allowing integration up to the wall, show realistic reproduction of the general mean flow pattern. The SMC, particularly with the improved model of Craft and Launder [11] for the pressure-reflection term, shows to be superior to the

KEM in capturing the strongly curved flow pattern in the corner regions, as well as in reproducing 3D effects owing to heat losses through the imperfectly insulated lateral walls. Despite several known deficiencies of both models used, the computational results are believed to yield useful qualitative information about the predictive performance of each class of models in enclosed side-heated buoyancy-driven flows.

2. Because of needs to integrate the equations up to the wall and to resolve thin boundary layers with a sufficiently fine computational grid, the 3D
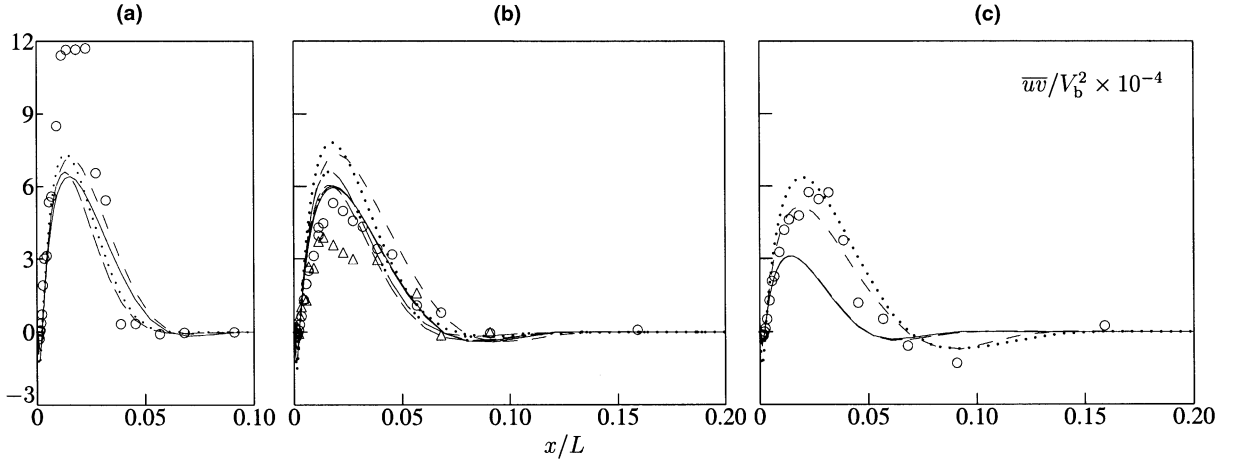
Fig. 16. The turbulent shear stress $\overline{uv}/V_b^2$ at $y/H = 0.5$ (a), $y/H = 0.7$ (b) and $y/H = 0.9$ (c). The symbols are measurements at $z/D = 0.5$ (○ = passive, △ = active case) and the lines are 2D computational results for isothermal horizontal walls (— = KEM, – – = SMC-CL) and 3D computations for the passive (- - = KEM, ⋯ = SMC-CL) and active case (—·— = KEM, —··— = SMC-CL).

computations are prohibitively tedious and computationally demanding. For computation of 3D complex internal buoyancy-driven flows, a middle-of-the route in the form of algebraic models, based on truncation of here considered or other differential SMCs, may be more suitable for the time being.

Acknowledgements

Appendix A. Second-moment closure model

This appendix lists the equations, functions and constants used for the SMC-PH of Peeters and Henkes [10] and the impinging-jet correction of Craft and Launder [11], which is referred to as SMC-CL when applied to the SMC-PH.

A.1. SMC-PH

$$\frac{D\overline{u_i u_j}}{Dt} = \frac{\partial}{\partial x_k}\left[\left(v\delta_{kl} + c_s\frac{k}{\varepsilon}\overline{u_k u_l}\right)\frac{\partial \overline{u_i u_j}}{\partial x_l}\right]$$
$$+ P_{ij} + G_{ij} + \Pi_{ij} - \varepsilon_{ij} + E_{ij},$$

$$\frac{D\overline{T'u_j}}{Dt} = \frac{\partial}{\partial x_k}\left[\left(\frac{1}{2}\{\alpha + v\}\delta_{kl} + c_T\frac{k}{\varepsilon}\overline{u_k u_l}\right)\frac{\partial \overline{T'u_j}}{\partial x_l}\right]$$
$$+ P_{Tj}^{th} + P_{Tj}^{m} + G_{Tj} + \Pi_{Tj} + E_{Tj},$$

$$\overline{u_i u_j}|_w = \overline{T'u_j}|_w = 0.$$

$$\frac{D\varepsilon}{Dt} = \frac{\partial}{\partial x_k}\left[\left(v\delta_{kl} + c_\varepsilon\frac{k}{\varepsilon}\overline{u_k u_l}\right)\frac{\partial \varepsilon}{\partial x_l}\right]$$
$$+ \left[c_{\varepsilon1}f_{\varepsilon1}\left(\frac{1}{2}P_{kk} + c_{\varepsilon3}\frac{1}{2}G_{kk}\right) - c_{\varepsilon2}f_{\varepsilon2}\varepsilon\right]\frac{\varepsilon}{k} + E_\varepsilon,$$

$$\frac{D\overline{T'^2}}{Dt} = \frac{\partial}{\partial x_k}\left[\left(\alpha\delta_{kl} + c_{TT}\frac{k}{\varepsilon}\overline{u_k u_l}\right)\frac{\partial \overline{T'^2}}{\partial x_l}\right] + P_{TT} - \varepsilon_{TT} + E_{TT},$$

$$\frac{D\varepsilon_{TT}}{Dt} = \frac{\partial}{\partial x_k}\left[\left(\alpha\delta_{kl} + c_{\varepsilon TT}\frac{k}{\varepsilon}\overline{u_k u_l}\right)\frac{\partial \varepsilon_{TT}}{\partial x_l}\right]$$
$$+ (c_{P1}P_{TT} - c_{D1}\varepsilon_{TT})\frac{\varepsilon_{TT}}{\overline{T'^2}}$$
$$+ \left(c_{P2}\frac{1}{2}P_{kk} - c_{D2}\varepsilon\right)\frac{\varepsilon_{TT}}{k},$$

$$\varepsilon|_w = \overline{T'^2}|_w = \varepsilon_{TT}|_w = 0.$$

$$P_{ij} = -\overline{u_k u_j}\frac{\partial U_i}{\partial x_k} - \overline{u_k u_i}\frac{\partial U_j}{\partial x_k}, \quad G_{ij} = -g_i\beta\overline{T'u_j} - g_j\beta\overline{T'u_i},$$

$$P_{Tj}^{th} = -\overline{u_j u_k}\frac{\partial T}{\partial x_k}, \quad P_{Tj}^{m} = -\overline{T'u_k}\frac{\partial U_j}{\partial x_k},$$

$$G_{Tj} = -g_j\beta\overline{T'^2}, \quad P_{TT} = -2\overline{T'u_k}\frac{\partial T}{\partial x_k},$$

$$\varepsilon_{ij} = (1 - f_s)\frac{2}{3}\varepsilon\delta_{ij} + f_s\frac{\varepsilon}{k}\overline{u_i u_j}, \quad f_s = \frac{1}{1 + Re_t/10},$$

$$E_{ij} = \begin{cases} -2v\frac{\overline{u_i u_j}}{x_n^2}, & i = j, \\ -2v\frac{\overline{u_i u_j} + \overline{u_i u_k}n_k n_j + \overline{u_j u_k}n_k n_i + \overline{u_k u_l}n_k n_l n_i n_j}{x_n^2}, & i \neq j, \end{cases}$$

$$E_{Tj} = -(\alpha + v)\frac{\overline{T'u_j} + \overline{T'u_k}n_k n_j}{x_n^2}, \quad E_{TT} = -2\alpha\frac{\overline{T'^2}}{x_n^2},$$

$$f_{\varepsilon2} = 1 - \frac{2}{9}\exp\left[-\left(\frac{Re_t}{6}\right)^2\right], \quad Re_t = \frac{k^2}{v\varepsilon},$$

$$c_{\varepsilon3} = \tanh|\cot\theta|, \quad \theta = \angle(U_i, g_i),$$

$$E_\varepsilon = -2v\frac{\varepsilon}{x_{\mathrm{n}}^2}\exp(-0.5x_{\mathrm{n}}^+), \quad x_{\mathrm{n}}^+ = x_{\mathrm{n}}\frac{U_\tau}{v},$$

$$U_\tau = \left(v\left|\frac{\partial U_{\mathrm{p}}}{\partial x_{\mathrm{n}}}\right|_{\mathrm{w}}\right)^{1/2}.$$

$$\Pi_{ij} = \Pi_{ij,1} + \Pi_{ij,2} + \Pi_{ij,3} + \Pi_{ij,1}^{\mathrm{w}} + \Pi_{ij,2}^{\mathrm{w}},$$

$$\Pi_{Tj} = \Pi_{Tj,1} + \Pi_{Tj,2} + \Pi_{Tj,3} + \Pi_{Tj,1}^{\mathrm{w}},$$

$$\Pi_{ij,1} = -c_1\frac{\varepsilon}{k}\left(\overline{u_iu_j} - \frac{2}{3}k\delta_{ij}\right),$$

$$\Pi_{ij,2} = -c_2\left(P_{ij} - \frac{1}{3}P_{kk}\delta_{ij}\right), \quad \Pi_{ij,3} = -c_3\left(G_{ij} - \frac{1}{3}G_{kk}\delta_{ij}\right),$$

$$\Pi_{ij,1}^{\mathrm{w}} = c_1^{\mathrm{w}}\frac{\varepsilon}{k}\left(\overline{u_ku_l}n_kn_l\delta_{ij} - \frac{3}{2}\overline{u_iu_k}n_kn_j - \frac{3}{2}\overline{u_ju_k}n_kn_i\right)f_{\mathrm{w}},$$

$$\Pi_{ij,2}^{\mathrm{w}} = c_2^{\mathrm{w}}\left(\Pi_{kl,2}n_kn_l\delta_{ij} - \frac{3}{2}\Pi_{ik,2}n_kn_j - \frac{3}{2}\Pi_{jk,2}n_kn_i\right)f_{\mathrm{w}},$$

$$\Pi_{Tj,1} = -c_{1T}\frac{\varepsilon}{k}\overline{T'u_j},$$

$$\Pi_{Tj,2} = -c_{2T}P_{Tj}^{\mathrm{m}}, \quad \Pi_{Tj,3} = -c_{3T}G_{Tj},$$

$$\Pi_{Tj,1}^{\mathrm{w}} = c_{1T}^{\mathrm{w}}\Pi_{Tk,1}f_{\mathrm{w}}n_kn_j, \quad f_{\mathrm{w}} = \frac{k^{3/2}}{c_{\mathrm{w}}\varepsilon l_{\mathrm{I}}},$$

$$\frac{1}{l_{\mathrm{I}}} = \frac{1}{4}\int_{\varphi\langle\pi\rangle}\int_{\theta\langle2\pi\rangle}\frac{\mathrm{d}\theta\,\mathrm{d}\varphi}{l(\theta,\varphi)}.$$

$c_{\varepsilon1}$	$c_{\varepsilon2}$	$f_{\varepsilon1}$	c_{s}	c_T	c_ε
1.35	1.80	1	0.20	0.20	0.15

c_{TT}	$c_{\varepsilon TT}$	c_{P1}	c_{D1}	c_{P2}	c_{D2}
0.22	0.22	1.8	2.2	0.72	0.8

c_1	c_2	c_3	c_1^{w}	c_2^{w}
2.2	0.55	0.55	0.6	0.3

c_{1T}	c_{2T}	c_{3T}	c_{1T}^{w}	c_{w}
3.75	0.5	0.5	0.2	2.53

A.2. SMC-CL

$$\Pi_{ij,2}^{\mathrm{w}} = -0.08\frac{\partial U_k}{\partial x_l}\overline{u_ku_l}(\delta_{ij} - 3n_in_j)f_{\mathrm{w}} - 0.1ka_{kl}$$
$$\times\left(\frac{\partial U_m}{\partial x_l}n_kn_m\delta_{ij} - \frac{3}{2}\frac{\partial U_i}{\partial x_l}n_kn_j - \frac{3}{2}\frac{\partial U_j}{\partial x_l}n_kn_i\right)f_{\mathrm{w}}$$
$$+ 0.4k\frac{\partial U_k}{\partial x_l}n_kn_l(n_in_j - \delta_{ij}/3)f_{\mathrm{w}}, \quad a_{ij} = \frac{\overline{u_iu_j}}{k} - \frac{2}{3}\delta_{ij}.$$

In the above equation for l_{I}, θ runs through a horizontal plane intersecting the fixed point where l_{I} is to be determined, φ runs through a side half of the vertical plane intersecting the mentioned point and the mentioned horizontal plane at angle θ, and l is the distance between the fixed internal point and the running wall point.

References

[1] R.A.W.M. Henkes, C.J. Hoogendoorn (Eds.), in: Proceedings of the EUROTHERM Seminar 22: Turbulent Natural Convection in Enclosures, EETI (France), Delft, The Netherlands, 1992.

[2] H.S. Dol, K. Hanjalić, S. Kenjereš, A comparative assessment of the second-moment differential and algebraic models in turbulent natural convection, Int. J. Heat Fluid Flow 18 (1997) 4–14.

[3] K. Hanjalić, Achievements and limitations in modelling and computation of buoyant turbulent flows and heat transfer, Special keynote lecture, in: G.F. Hewitt (Ed.), in: Proceedings of the 10th International Heat Transfer Conference, vol. 1, Brighton, UK, IChemE, Taylor & Francis, London, 1994, pp. 1–18.

[4] S. Kenjereš, Numerical modelling of complex buoyancy-driven flows, Ph.D. thesis, Delft University of Technology, Delft, The Netherlands, 1999.

[5] H.S. Dol, K. Hanjalić, T.A.M. Versteegh, A DNS-based thermal second-moment closure for buoyant convection at vertical walls, J. Fluid Mech. 391 (1999) 211–247.

[6] I.J. Opstelten, Experimental study on transition characteristics of natural-convection flow, Ph.D. thesis, Delft University of Technology, Delft, The Netherlands, 1994.

[7] H.S. Dol, I.J. Opstelten, K. Hanjalić, Turbulent natural convection in a side-heated near-cubic enclosure: experiments and model computations, Technical report APTF R/00-02, Thermal and Fluids Science Section, Department of Applied Physics, Delft University of Technology, Delft, The Netherlands, 2000.

[8] R. Cheesewright, K.J. King, S. Ziai, Experimental data for the validation of computer codes for the prediction of two-dimensional buoyant cavity flows, in: Proceedings of the ASME Winter Annual Meeting, vol. HTD-60, Anaheim, Brea, CA, 1986, pp. 75–81.

[9] K.J. King, Turbulent natural convection in rectangular air cavities, Ph.D. thesis, Queen Mary College, London, UK, 1989.

[10] T.W.J. Peeters, R.A.W.M. Henkes, The Reynolds-stress model of turbulence applied to the natural-convection boundary layer along a heated vertical plate, Int. J. Heat Mass Transfer 35 (1992) 403–420.

[11] T.J. Craft, B.E. Launder, New wall-reflection model applied to the turbulent impinging jet, AIAA J. 30 (1992) 2970–2972.

[12] K.-Y. Chien, Predictions of channel and boundary-layer flows with a low-Reynolds-number turbulence model, AIAA J. 20 (1982) 33–38.

[13] C. Hirsch, Numerical Computation of Internal and External Flows, vol. 2, Wiley, Chichester, UK, 1994.

[14] B. Van Leer, Towards the ultimate conservative difference scheme. II. Monotonicity and conservation combined in a second order scheme, J. Comp. Phys. 14 (1974) 361–370.

[15] H.S. Dol, Turbulence models for natural convection in side-heated enclosures, Ph.D. thesis, Delft University of Technology, Delft, The Netherlands, 1998.

[16] N.Z. Ince, B.E. Launder, On the computation of buoyancy-driven turbulent flows in rectangular enclosures, Int. J. Heat Fluid Flow 10 (1989) 110–117.

[17] M.M. Gibson, B.E. Launder, Ground effects on pressure fluctuations in the atmospheric boundary layer, J. Fluid Mech. 86 (1978) 491–511.

[18] B.E. Launder, Heat and mass transport in turbulence, in: P. Bradshaw (Ed.), Topics in Applied Physics, Springer, Berlin, 1976.

[19] K. Hanjalić, B.E. Launder, Contribution towards a Reynolds-stress closure for low-Reynolds-number turbulence, J. Fluid Mech. 74 (1976) 593–610.

[20] H.S. Dol, K. Hanjalić, S. Kenjereš, A comparative assessment of the second-moment differential and algebraic models in turbulent natural convection, in: Proceedings of the Turbulent Heat Transfer Conference, Engineering Foundation, New York, San Diego, USA, 1996.

[21] R.J.A. Janssen, Instabilities in natural-convection flows in cavities, Ph.D. thesis, Delft University of Technology, Delft, The Netherlands, 1994.

[22] T. Tsuji, Y. Nagano, Turbulence measurements in a natural convection boundary layer along a vertical flat plate, Int. J. Heat Mass Transfer 31 (1988) 2101–2111.

[23] R.A.W.M. Henkes, C.J. Hoogendoorn, Comparison of turbulence models for the natural convection boundary layer along a heated vertical plate, Int. J. Heat Mass Transfer 32 (1989) 157–169.

[24] R.A.W.M. Henkes, Application of k–ε models to the transition of natural-convection boundary layers, in: R.M.C. So, C.G. Speziale, B.E. Launder (Eds.), Near-Wall Turbulent Flows, Elsevier, Amsterdam, 1993, pp. 177–186.

[25] N.Z. Ince, B.E. Launder, Three-dimensional and heat-loss effects on turbulent flow in a nominally two-dimensional cavity, Int. J. Heat Fluid Flow 16 (1995) 171–177.